

3D versus 2D Electrolyte–Semiconductor Interfaces in Rylenediimide-Based Electron-Transporting Water-Gated Organic Field-Effect Transistors

Federico Prescimone, Emilia Benvenuti, Marco Natali, Andrea Lorenzoni, Franco Dinelli, Fabiola Liscio, Silvia Milita, Zhihua Chen, Francesco Mercuri, Michele Muccini, Antonio Facchetti, and Stefano Toffanin*

Water-gated organic field-effect transistors (WGOFETs) are relevant devices for use in the fields of biosensors and biosystems. However, real applications require very stringent performance in terms of electrochemical stability and charge mobility to the organic semiconductor in contact with an aqueous environment. Here, a comparative study of two small-molecule electron-transporting perylene diimide semiconductors, which differ only in the *N*-substituents named PDIF-CN₂ and PDI8-CN₂ is reported. The two materials present similar solid-state arrangements but, while the PDI8-CN₂ shows a more 3D growth modality and electron mobility independent of the semiconductor layer thickness ($\approx 10^{-4} \text{ cm}^2 \text{ V}^{-1} \text{ s}^{-1}$), the PDIF-CN₂ has an almost-2D growth modality and the mobility increases with the semiconductor film thickness, reaching a maximum value of $\approx 5 \times 10^{-3} \text{ cm}^2 \text{ V}^{-1} \text{ s}^{-1}$ at 30 nm. Above this thickness, the PDIF-CN₂ switches to a more 3D growth modality, and the mobility drops by one order of magnitude. XRR analysis indicates that a PDIF-CN₂ film can be modeled as a dense layered structure in which each layer is decoupled from the others due to the presence of fluorocarbon-chains. The availability of additional pathways for charge transport from buried layers and the 2D versus 3D growth can explain the mobility dependence on the film thickness.


aqueous electrolyte solution acting as the gate dielectric in contact with the organic semiconductor (OS).^[1,2] This kind of architecture enables the WGOFET to transduce bioelectrical signals and to detect molecular analytes, ions, and biomarkers.^[1,3,4] In WGOFETs the charge accumulation in the OS is caused by the electrolyte ions migrating close to the OS interface and to the gate interface when a gate potential is applied.^[5,6] Thus, charge accumulation in the OS film and charge transport occur close to OS/electrolyte interface. In this scenario, the structural organization and the morphological features of the OS/electrolyte interface play a crucial role in the device performance, as expected in any class of field-effect transistors based on thin films. The growth mechanism of the active layer as the thin-film layer thickness is increased typically controls the film morphology and molecular organization of the interface that is finally exposed to water, as it is in the case of standard OFET devices with a top-gate configuration.^[6–8] Among the plethora of organic semiconductors

with different molecular structures and tailored electrical properties, thin films comprised by linear molecular systems, like pentacene and α -sexithiophene, are subjected to a transition from a layer-by-layer to island growth upon completion of a few molecular monolayers (5–6 nm).^[9–12] This growth mechanism

1. Introduction

Water-gated organic field-effect transistors (WGOFETs) are considered an intriguing class of electronic devices for biosensing given that the gate electrode is immersed in an

F. Prescimone, Dr. E. Benvenuti, Dr. M. Natali, Dr. A. Lorenzoni, Dr. F. Mercuri, Dr. M. Muccini, Dr. S. Toffanin
Istituto per lo Studio dei Materiali Nanostrutturati (ISMN)—Consiglio Nazionale delle Ricerche (CNR)
Via Gobetti 101, Bologna 40129, Italy
E-mail: stefano.toffanin@cnr.it

 The ORCID identification number(s) for the author(s) of this article can be found under <https://doi.org/10.1002/aelm.202000638>.

© 2020 The Authors. Advanced Electronic Materials published by Wiley-VCH GmbH. This is an open access article under the terms of the Creative Commons Attribution License, which permits use, distribution and reproduction in any medium, provided the original work is properly cited.

DOI: 10.1002/aelm.202000638

Dr. F. Dinelli
Istituto Nazionale di Ottica (INO)—Consiglio Nazionale delle Ricerche (CNR)
Via Giuseppe Moruzzi 1, Pisa 56127, Italy

Dr. F. Liscio, Dr. S. Milita
Istituto per la Microelettronica e i Microsistemi (IMM)—Consiglio Nazionale delle Ricerche (CNR)
Via Gobetti 101, Bologna 40129, Italy

Dr. Z. Chen
Flexterra Inc.
8045 Lamon Avenue, Skokie, IL 60077, USA

Dr. A. Facchetti
Department of Chemistry and the Material Research Center
Northwestern University
633 Clark Street, Evanston, IL 60208-3113, USA

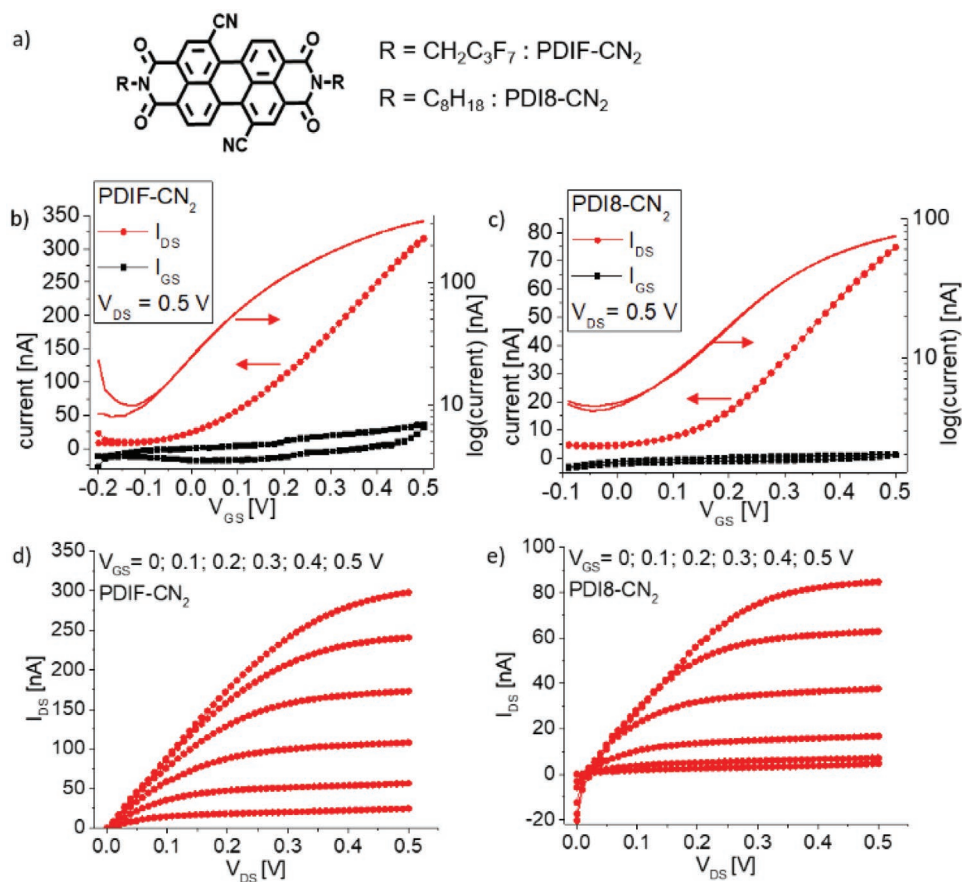


Figure 1. a) Molecular structures of the two organic semiconductors, namely PDIF-CN₂ and PDI8-CN₂. b,c) Electrical characteristics: saturation transfer curves (STCs) and d,e) multiple output curves (MOCs) of one representative WGOFET for b,d) 30 nm thick PDIF-CN₂ and c,e) PDI8-CN₂ active layers. In the STCs, the source-drain current (I_{DS}) is collected by sweeping the top gate-source voltage (V_{GS}) from -0.2 to 0.5 V while keeping the drain-source voltage (V_{DS}) constant at 0.5 V and the conductive substrate connected to ground; the dotted plots represent the I_{DS} current and refer to left y-axis, while line plot is the logarithmic of the I_{DS} current and refers to a right y-axis. In the MOCs, I_{DS} is collected by sweeping V_{DS} from 0 to 0.5 V and V_{GS} from 0 to 0.5 V with a step of 0.1 V. Source-gate current (I_{GS} , leakage currents) are also reported in (b) and (c) (black square points).

is typically correlated with an increase of surface roughness and reduction of the inter-island connection in the outermost layers of the thicker organic films.^[13,14] This feature might not affect the field-effect charge mobility in OFETs in bottom-gate configuration since the charge transport in the OS is located at the lower interface with the solid dielectric layer. However, in WGOFETs the capacitive coupling between water and the OS is located exactly at the outermost layers: mastering at the μm -length scale the structural organization and the morphological features of the OS active layer at the interface with the electrolyte is essential for the performance optimization of electrolyte-gated transistors. Indeed, it has been reported that the carrier mobility drops in thick-film based WGOFETs with respect to corresponding bottom-gate/bottom-contact OFETs counterpart because of morphological inhomogeneities of the interface in contact with the electrolyte.^[5,15]

In this scenario, organic small molecules are good candidates for correlating molecular structure of the constituting moieties, the solid-state packing, and the electrical performance of the device since the active layer film growth modality can be easily controlled via different deposition protocols.^[16–21] A mandatory criterion for using an OS as the active layer in

WGOFET devices is stability in water conditions. The use of electron-transporting materials in WGOFETs is strictly limited by the typical lowest unoccupied molecular orbital (LUMO) levels, which render these materials unstable in presence of air/O₂/H₂O. A specific class of electron-transporting organic semiconductors, the cyano-substituted perylene-diimides (PDI) derivatives, has been reported to fulfill this requirement since the presence of high electron-withdrawing CN groups on the aromatic core optionally in combination with *N*-perfluorocarbon chains lowers the LUMO energy.^[22,23] Specifically, *N,N'*-1*H*,1*H*-perfluorobutyl-dicyanoperylene-3,4:9,10-bis(dicarboximide) (PDIF-CN₂, FlexterraActivInk N1100, see Figure 1a) is a promising candidate as active layer in WGOFET given that this compound presents optimized LUMO energy level for air-stability (-4.5 eV) and high electron FET mobility ($\approx 10^{-1}$ cm² V⁻¹ s⁻¹) in thin-film bottom-gate bottom-contact configuration.^[22,24] To correlate the electrical behavior of PDIF-CN₂ in a device configuration with its molecule chemical functionalities and the morphological/structural arrangement of the OS/electrolyte interface, *N,N'*-bis(*n*-octyl)-*x,y*-dicyanoperylene-3,4:9,10-bis(dicarboximide) (PDI8-CN₂, FlexterraActivInk N1200, see Figure 1a) is used as a reference system since this

molecule presents similar i) steric hindrance, ii) LUMO energy level (-4.3 eV), and iii) out-of-plane packing when deposited as thin films. Moreover, the two molecules have the same molecular structures but differ only in the chemical nature of the *N*-substituents: longer (C_8) alkyl chains (RH) for PDI8-CN₂ and shorter (C_4) and partially fluorinated chains (RF) for PDIF-CN₂. Interestingly, both molecules organize in a compact edge-on structure that leads the *N*-substituents to be exposed at the outer surface.^[24,25] Here, we report on the electron-transporting field-effect lateral transport of thermally evaporated PDIF-CN₂ and PDI8-CN₂ films in WGOFET devices. The main molecular, energetic, and long-range organization factors modulating the charge transport and device operation are studied. In particular, the molecular organization, growth mechanisms and energetics of the OS/water interface are correlated to the mobility of the WGOFET devices as the thickness of the active layer is increased. In the case of PDIF-CN₂, the maximization of the charge mobility at large OS film thickness is linked to the preservation of a quasi-2D stacking of molecular layers in the direction normal to the substrate. On the other hand, electron mobility of PDI8-CN₂ saturates after 1–2 monolayers from the OS/water interface due to the prevalent 3D growth modality at large film thickness. The different growth modality of the two perylene-based derivatives is the major factor at the basis of the one-order-of magnitude higher electron mobility of the PDIF-CN₂ with respect to PDI8-CN₂.

2. Results and Discussion

2.1. Performance of PDI-Based Water-Gate Organic Field-Effect Transistors

The WGOFET devices are fabricated in a bottom-contact top-gate configuration using PDIF-CN₂ and PDI8-CN₂ as active layer (see Figure 1a for the chemical structures of the compounds) and ultrapure deionized water as electrolyte and a thin platinum wire (diameter 0.5 mm) as the gate electrode. The semiconductor films are deposited by high-vacuum sublimation onto Si/SiO₂ substrate functionalized with hexamethyldisilazane. Moreover, the source/drain gold injecting-electrodes are functionalized by 4-chlorobenzenemethanethiol self-assembling monolayer prior to semiconductor deposition (see the Experimental Section).

During the sublimation the substrate is heated at 90 °C. Figure 1 shows representative saturation transfer curves (STC, Figure 1b,c) and the multiple output curves (MOCs, Figure 1d,e) of WGOFETs based on 30 nm thick PDIF-CN₂ and PDI8-CN₂ films. During the electrical measurements the Si/SiO₂ substrate is grounded and the electrical characteristics are collected when the device is operated at low voltage (from -0.2 to 0.5 V) to avoid water redox reactions and thus the possibility of extensive electrochemical doping of the active layer.^[1] Indeed, the absence of hysteresis between forward and reverse sweeps in the *I*–*V* curves and the almost negligible leakage currents (i.e., units of nA in the source-gate currents in Figure 1b,c) confirm the absence of massive ion percolation from water into the OS bulk suggesting the stable formation of the electrical double layer.^[5,26,27]

Both semiconductors show a field-effect behavior in a water-gated configuration. The values of the electron charge mobility are extrapolated from the transfer curves in the saturation regime once the values of the capacitance of Debye–Helmholtz double layer (C_{DL}) are known. These values are obtained by performing standard electrochemical impedance spectroscopy (EIS) for the two different semiconductors in a metal-OS-water-metal structure. In order to increase the fitting quality, the equivalent circuit model implemented for fitting the collected impedance curves is an extension of the Randles equivalent model (see the Supporting Information, for details about the complete equivalent circuit model and correlated Figure S1, Supporting Information). The fitting of the impedance curves highlights that the leakage resistance (RL) that might be correlated to ion percolation in the OS is very high, proving that water percolation inside the OS is negligible as expected for WGOFETs working at a low voltage range.^[26] The extracted values of C_{DL} for both compounds are about $4 \mu\text{F cm}^{-2}$, well-aligned with the reported values for most organic semiconductors (either small molecules or polymers) used in water-gated transistors.^[1] By using the as-measured double-layer capacitance in the analysis of the 30 nm-thick WGOFETs (Figure 1), PDIF-CN₂ exhibits one-order-of-magnitude larger electron mobility ($1.2 \times 10^{-3} \text{ cm}^2 \text{ V}^{-1} \text{ s}^{-1}$), as well as source-drain current (≈ 350 nA), with respect to those of PDI8-CN₂. The electrical performance of PDIF-CN₂ in terms of charge mobility is in line with the values reported in literature for organic polymer/small molecule semiconductors, such as P3HT, $\alpha 6\text{T}$, pBTTT, rubrene, and pentacene with Pt or Ag/AgCl gate electrode and polymers, such as PNDIT2, PNDISVS, and PCBM with a tungsten gate electrode.^[1,6,28–32] Conversely, PDI8-CN₂ based WGOFETs are much less performing with charge mobility of $2.9 \times 10^{-4} \text{ cm}^2 \text{ V}^{-1} \text{ s}^{-1}$. When PDIF-CN₂ and PDI8-CN₂ vacuum-sublimed thin films are used as active layers in a standard OFETs (i.e., typically bottom-gate/bottom-electrode configuration) by using a solid-state dielectric, the electron mobility might reach values in the range of 10^{-1} and $10^{-2} \text{ cm}^2 \text{ V}^{-1} \text{ s}^{-1}$, respectively.^[24,33,34] As we outlined in Section 1, the charge mobility reduction is typically expected when the OS is implemented as active layer in WGOFETs since the outermost organic surface coupling with the electrolyte is more defective and poorly connected with respect to OS/solid-state dielectric interface in bottom configuration.^[5]

We highlight that the nonideality of the FET characteristics such as $V_{th} < 0$ V (about -0.19 V for PDIF-CN₂ and -0.05 V for PDI8-CN₂ both extrapolated from the saturation regime in STCs) has already been reported in literature for rylene diimide-based FET devices.^[33,35] In particular, this phenomenon may be attributed to the unintentional doping by chemical moieties.^[36] Moreover, we observe that the FET characteristics of PDI8-CN₂ based WGOFET is affected by the nonlinear contribution of the contact resistance (R_C) at low V_{DS} , even though the device gold injecting-electrodes of all the as-realized devices were treated by thiol-functionalization (see the Experimental Section).^[37] In particular, it has been reported that the functionalization of the gold electrodes with a 4-chlorobenzenemethanethiol self-assembling monolayer in a bottom-contact/bottom-gate device configuration is expected to reduce by only a factor between 30% and 15% (depending on the film thickness) the typical R_C values

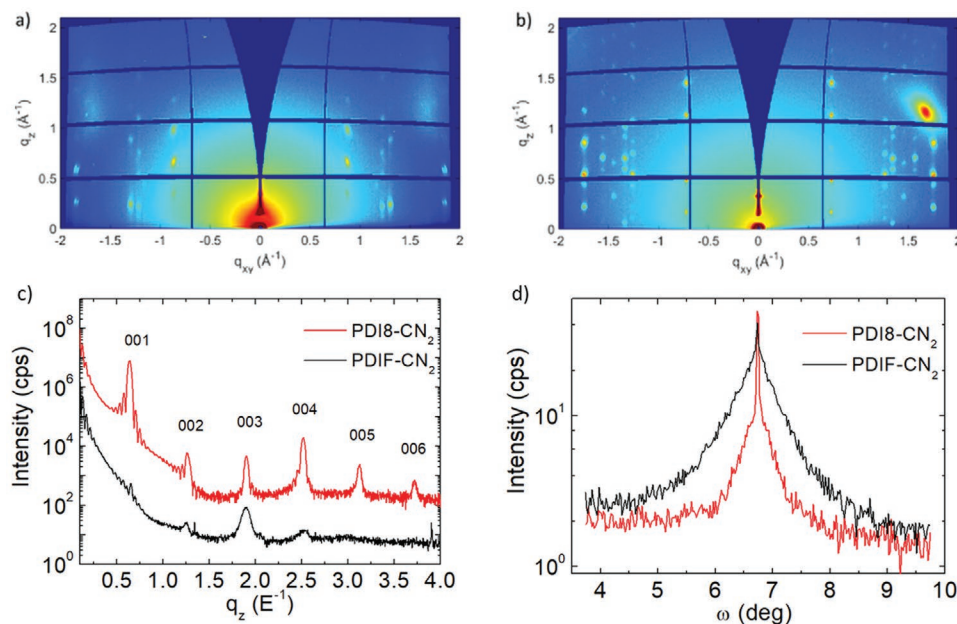


Figure 2. 2D-GIXD of 30 nm thick thin films of a) PDIF-CN₂ and b) PDI8-CN₂. c) XRD specular scans and d) (003) rocking curves of 30 nm thick films for both compounds.

of about 100 and 40 kΩ cm for PDI8-CN₂ and PDIF-CN₂, respectively.^[24,38]

Even though the specific voltage polarization conditions and device configuration used in this work must be explicitly considered for a proper quantification of the contact resistance contribution, it is plausible that in the present case the morphological issues related to a possible defective growth mode of the semiconducting film in the vicinity of the functionalized electrodes (as a consequence of the deposition of the organic layer onto pre-patterned electrodes) tend to play a major role in determining the final R_C values, especially in the case of PDI8-CN₂.^[24]

To check the possible correlation between the molecular packing of the organic semiconductors and the electrical performance of the FET device, the 30 nm thick PDIF-CN₂ and PDI8-CN₂ films were studied by X-ray diffraction (XRD) both in Grazing Incidence and specular geometries. 2D Grazing-incidence X-ray diffraction (2D-GIXD) images reported in **Figure 2a,b** show Bragg reflections consistent with the reported single-crystal structures having the molecules arranged in an *edge-on* configuration with the long molecular axes aligned almost perpendicular to the film plane.^[21,22,39–41] This configuration is confirmed by the specular scans, where only the (00*l*) reflections are detected for both films (**Figure 2c**), and where the well-defined Laue oscillations indicate the homogeneous vertical stacking of the molecular layers. The narrower Bragg peaks for PDI8-CN₂ film points out that PDI8-CN₂ crystal domains are larger than the PDIF-CN₂ ones. The Rocking Curves (RC) collected around the 003 reflection (**Figure 2d**) are characterized by the overlap of two components: i) a very narrow peak, the same for both the systems, which is related to highly textured film, being the full width at half-maximum (FWHM), an indication of the film mosaicity; ii) a broader peak (diffuse scattering) whose area is proportional to the amount of

crystalline defects. Interestingly, despite the crystalline defects are more numerous in the PDIF-CN₂ film, it has higher charge mobility in WGO-FET device. Although the charge mobility in FETs is normally related to the crystallinity and to the density of defects in the semiconductor film, as we report in the following, other factors must be invoked to fully explain the device performance.^[42,43]

2.2. Dependence of the Spatial Distribution of Water Molecules on the N-Substituents at the Water/PDI-Semiconductor Interfaces

XRD measurements show that both molecules arrange on the SiO₂/Si substrate exposing the linear chains to water leaving the π -conjugated molecular cores decoupled with respect to the water dipoles at the OS/water interface. Thus, water-induced polaron trap-state formation at the organic-side of the semiconductor/water interface can be excluded for both molecules. However, a different packing and superficial energy of the OS top surface in contact with water are plausible for the two semiconductors due to the different nature of the N-substituents. Indeed, the larger dipole moment of the CF bond with respect to CH bond may induce a stronger interaction with the water dipole. In this regard, the molecular arrangement of the OS/water interface was further investigated by molecular dynamics (MD) simulations. Models of the two layers of PDI8-CN₂ and PDIF-CN₂, in contact with bulk water, were equilibrated at room temperature (see Supporting Information for model details). Despite a more packed structure of the PDIF-CN₂ in the bulk crystal with respect to the PDI8-CN₂, the analysis of the equilibrated MD trajectories suggests a different organization of the side chains at the surface (**Figure 3**).^[40] Namely, PDIF-CN₂ exhibits a larger spacing between the side chains along the

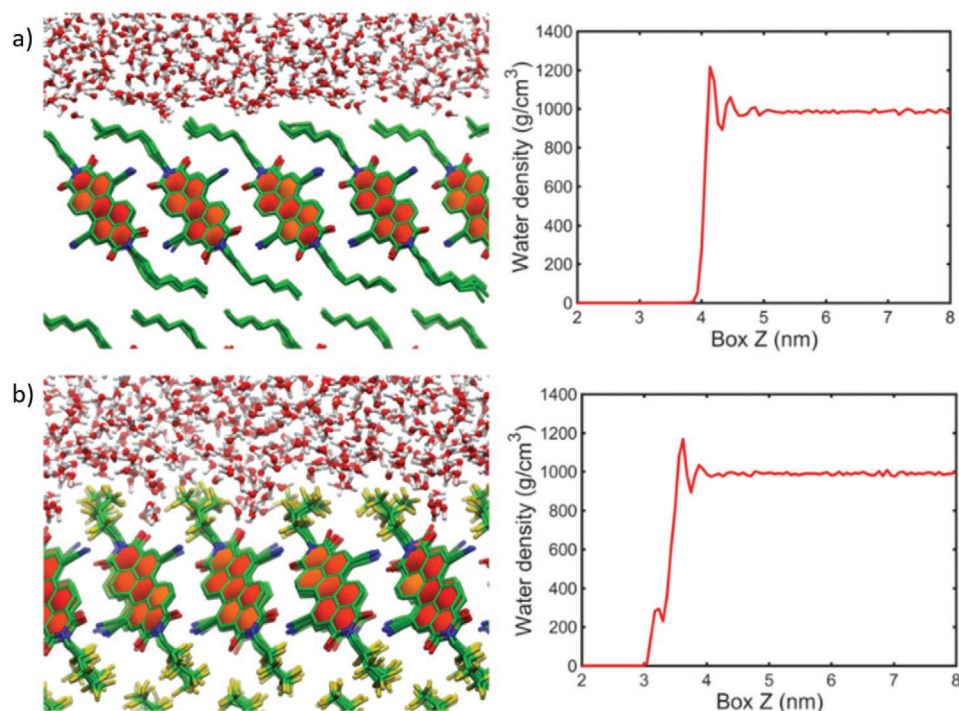


Figure 3. Left: snapshots are taken from MD simulation of water at the equilibrium with a) PDI8-CN₂ and b) PDIF-CN₂ layers. Right: density profile of water molecules along the direction orthogonal to the organic layer; the mean in plane position of the topmost atoms of the second topmost molecular layer is taken as reference ($Z = 0$).

in-plane direction due to their shorter chain length and to the repulsive interaction between the F atoms. PDI8-CN₂, instead, maintains the same packing at the surface as in the bulk, as evidenced by the ordered and aligned pattern of the alkyl chains in contact with the water layer (Figure 3a). The different morphologies lead to a different organization of water molecules at the interface with the organic layers (Figure 3a,b left). However, the computed average component of the dipole moment of water molecules, orthogonal to the interface (z -axis), is essentially identical for the two materials, as shown in Figure S2a (Supporting Information). Moreover, the experimental measures of contact angle captured on a 30 nm thick film corroborate MD simulation's results because the two materials display similar hydrophobic properties, i.e., contact angle values of $98.0^\circ \pm 1.8^\circ$ for PDIF-CN₂ and of $99.7^\circ \pm 1.9^\circ$ for PDI8-CN₂. Given that it is well known that the measures of contact angle are dependent on multiple surface-related parameters such as film morphology (see *infra*) which are strictly correlated with the deposition protocols of the OS thin films, we highlight that the measures of contact angle we collected in the case of PDIF-CN₂ are in line with literature for films deposited by the same method but lower with respect to films deposited by solution-processed technique.^[35,44] As expected, the computed distribution of the dipole moment reveals that only first and second water layers in contact with the surface are structured.^[45] Consequently, only a slight broadening of the molecular LUMO energy level (Figure S2b,c, Supporting Information) is expected from MD simulations. As a final remark, we can exclude that the more effective charge transport in PDIF-CN₂ based WGO-FETs is related to facilitated electrochemical doping.

2.3. Growth Modality and Mobility Dependence on Film Thickness

To explain the more performing FET behavior of PDIF-CN₂, we focused on investigating the correlation between the molecular packing, film morphology, and functionality of the solid-liquid interface for the two molecules. Specifically, we fabricated and characterized WGO-FET devices in which the semiconductor nominal thickness was varied from 5 to 50 nm. **Table 1** reports the FET performance parameters (source-drain current, electron mobility, and off-currents) as a function of the OS thickness. Other figures of merit and parameters of the as-realized devices such as threshold gate voltage, ON-OFF ratio and subthreshold swing are reported in Table S2 (Supporting Information).

For both molecules, the devices at 5 nm do not show an FET behavior due to a non-complete layer formation (**Figure 4**). In case of PDIF-CN₂, we observe that the charge mobility depends on the OS film thickness. In particular, the charge mobility and source-drain current values span one order of magnitude when the film thickness increases from 10 to 30 nm. On the other hand, PDI8-CN₂-based devices present mobility attesting around or less $5 \times 10^{-4} \text{ cm}^2 \text{ V}^{-1} \text{ s}^{-1}$ regardless of the thickness of the OS layer. To note that the values reported in Table 1 are obtained as average for all tested devices with the same thickness (4–10 devices for each thickness, see the Supporting Information for major details). As it can be seen in Figure S3 and Table S1 (Supporting Information), which reports the trend of PDIF-CN₂ and PDI8-CN₂ mobility average values as a function of film thickness and the corresponding bar errors defined as

Table 1. Comparison of the maximum source-drain currents ($I_{DS,max}$), electron mobility (μ) and off-current (I_{OFF}) values for PDIF-CN₂ and PDI8-CN₂ devices at different active layer thickness (from 5 to 50 nm). The values reported are the averages of the extracted parameters obtained from all the tested devices with the same thickness (4–10 tested devices). The reported parameters are derived from STCs in which I_{DS} is collected by sweeping the V_{GS} from -0.2 V to 0.5 V while keeping V_{DS} constant at 0.5 V and the conductive substrate connected to ground. The maximum source-drain current is collected at $V_{DS} = 0.5$ V and $V_{GS} = 0.5$ V.

Organic semiconductor	Thickness [nm]	$\langle I_{DS,max} \rangle$ [nA]	$\langle \mu \rangle$ [$\text{cm}^2 \text{V}^{-1} \text{s}^{-1}$]	$\langle I_{OFF} \rangle$ [nA]
PDIF-CN ₂	5	N/A	N/A	N/A
	10	89	1.4×10^{-4}	23
	20	637	7.1×10^{-4}	58
	30	728	1.1×10^{-3}	67
	40	530	2.5×10^{-4}	34
	50	7	8.6×10^{-6}	3
PDI8-CN ₂	5	N/A	N/A	N/A
	10	104	4.5×10^{-4}	2
	20	142	5.3×10^{-4}	2
	30	144	2.8×10^{-4}	4
	40	134	5.1×10^{-4}	8
	50	138	3.8×10^{-4}	5

standard deviation, the extracted mobility values can be considered reliable for both the materials regardless the extensively-reported variability of PDIF-CN₂ electrical performance.^[46,47] In this regard, we observe that all the tested PDIF-CN₂ based devices with 30 nm-thick active layer exhibit mobility in the range of $10^{-3} \text{ cm}^2 \text{V}^{-1} \text{s}^{-1}$, reaching $4.7 \times 10^{-3} \text{ cm}^2 \text{V}^{-1} \text{s}^{-1}$ in the best case whose STCs and MOCs are shown in Figure S4 (Supporting Information). As reported above for the devices shown in Figure 1, the major part of PDIF-CN₂ and PDI8-CN₂ devices

shows a negative threshold voltage (see Table S2, Supporting Information).^[36] Even though the detailed description of the nature of the threshold gate voltage in the rylenediimide derivatives is beyond the scope of this paper, we note that less-negative values for PDIF-CN₂ or even positive values for PDI8-CN₂ are obtained when the threshold gate voltage is extracted in the linear regime of the saturation transfer characteristics (Table S2, Supporting Information). As a further evidence of the possible unintentional doping of the rylenediimide-based semiconductors (especially PDIF-CN₂) is the high off-current (I_{OFF} values in Table 1) with respect to the state-of-the-art electrolyte-gated organic field-effect transistors.^[5,48] However, we cannot exclude that the geometry of the Pt wire used as gate electrode in the present work (i.e., larger diameter) might be partially responsible for the off-current and subthreshold swing values derived from the as-realized WGOFTs. A representative STC of each active-layer thickness value is reported in the Supporting Information (Figures S5 and S6). Differently from PDIF-CN₂, both charge mobility and source-drain current of PDI8-CN₂ based WGOFTs are independent of the OS layer thickness given that the mobility and currents values for each OS thickness are dispersed in a narrow range ($2.8\text{--}5.3 \times 10^{-4} \text{ cm}^2 \text{V}^{-1} \text{s}^{-1}$ and $100\text{--}150$ nA, respectively). The thickness-independent electrical performance is similar to what reported for pentacene or other organic semiconductors used in WGOFTs.^[1,49]

Despite that dependence of the source-drain current on the film thickness for PDIF-CN₂ might be a typical fingerprint of electrochemical doping as in the case of OECT devices, the values below the μA range together with the absence of hysteresis in STCs may safely exclude a massive ion percolation from water into the OS bulk.^[26] Characterization of the exposed upper-OS layer surface topography by means of atomic force microscopy (AFM) is performed at different film thicknesses (up to 30 nm) and is shown in Figure 4. AFM analysis is performed on the semiconductors deposited on functionalized Si/SiO₂ substrates and in the channel area of the devices.

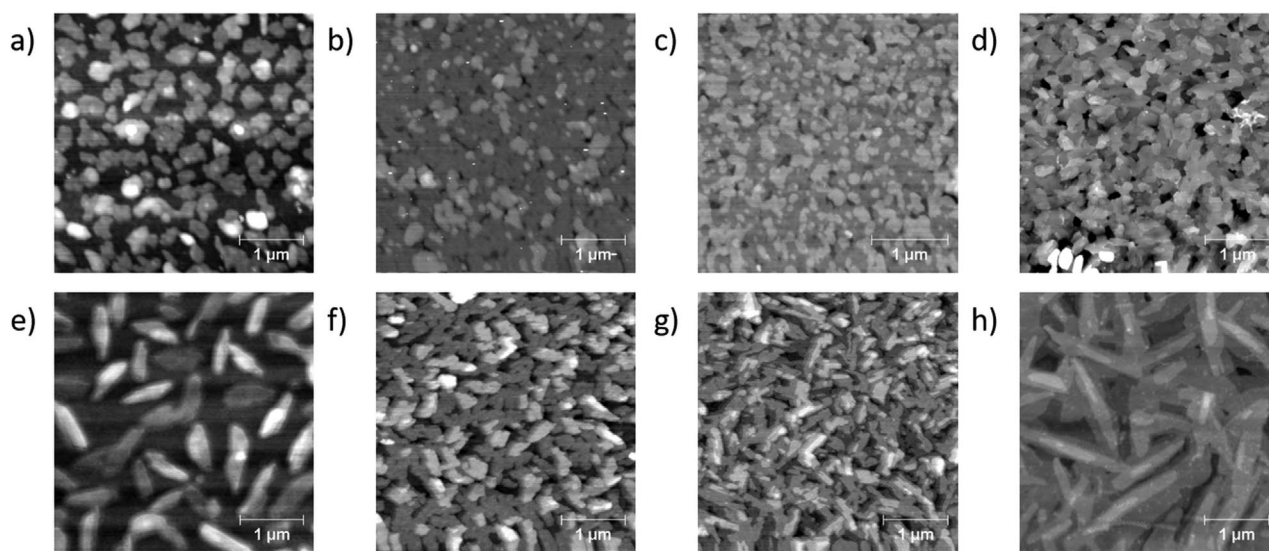


Figure 4. AFM images of PDIF-CN₂ (top) and PDI8-CN₂ (bottom) thin films grown at different thicknesses: a,e) 2 nm, b,f) 5 nm, c,g) 10 nm, and d,h) 30 nm.

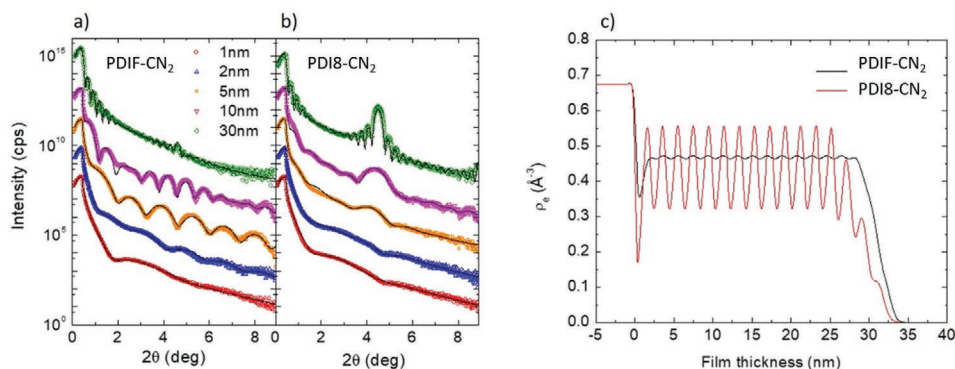


Figure 5. XRR experimental (dots) and fitting curves (solid lines) of a) PDIF-CN₂ and b) PDI8-CN₂ thin films with different thickness values (1, 2, 5, 10, and 30 nm). c) Electron density profile (ρ_e) of 30 nm thick PDIF-CN₂ and PDI8-CN₂ films resulting from the fit of the a,b) XRR curves.

AFM characterization suggests that the two semiconductor films grow with different mechanisms.^[24] When the OS thickness is below 5 nm the PDIF-CN₂ surface is characterized by the presence of disconnected small round terraces (diameter \approx 100–200 nm). Increasing the film thickness up to 10–15 nm, we observe the coexistence of two kinds of incomplete layers: an upper layer with flat small round terraces (diameter \approx 100–200 nm) with low layer-occupancy above an almost-complete layer that is characterized by the presence of well interconnected larger terraces with high layer-occupancy.^[50] Only a small increase of the root-mean-square roughness (σ) is observed by passing from 10 nm-thick layer ($\sigma = 0.96$ nm) to 20 nm ($\sigma = 1.33$ nm). When the thickness is 30 nm the uppermost layer is almost complete and no difference in RMS roughness is shown ($\sigma = 1.39$ nm). The depth line profile (see Figure S7, Supporting Information) extracted from the image of the 30 nm-thick film confirms that the round terraces are as high as the molecule length (\approx 2 nm), in line with the edge-one configuration found by XRD data. In this scenario, the AFM data suggest an almost layer-by-layer 2D growth mechanism for PDIF-CN₂.^[35] Differently, even the thinnest PDI8-CN₂ film shows the elsewhere-reported 3D structures.^[21,51] This structure is characterized by several low-occupancy incomplete layers with extended in-plane elongated (needle-like) grains whose length grows with the film thickness (see depth line profile present in Figure S7, Supporting Information). These needles are flat, have the height comparable to the length of PDI8-CN₂ (\approx 2 nm, in line with XRD results), and grow with the longer axis randomly oriented in the plane parallel to the substrate surface.^[35] The presence of voids due to the low grain-interconnection in PDI8-CN₂ films affects the quality of OS/water interface: the RMS roughness of PDI8-CN₂ films is slightly higher than PDIF-CN₂ ones, for equivalent thickness. On one hand, the values found for the devices with a 30 nm-thick semiconductor film (1.7 nm for PDI8-CN₂ vs 1.39 nm for PDIF-CN₂) are too similar to explain the considerable mobility difference between the two materials (one order of magnitude). On the other hand, similar values of RMS roughness for both materials deposited in 30-nm thick films are in line with the invariance of the values of contact angles for PDI8-CN₂ and PDIF-CN₂ that we reported in Section 2.2: as it has been reported

in literature, the surface wettability is strictly correlated with the film roughness.^[52] Therefore, σ is not the most suitable indicator to describe the different trends in FET mobility with the active layer thickness (Table 1).

2.4. Correlation Between Layered Packing and Enhanced Mobility in PDIF-CN₂

The origin of the enhanced mobility of PDIF-CN₂-based WGO-FETs can be investigated by characterizing the film growth modality (and consequently the packing motif) by using X-ray reflectivity (XRR) measurements. XRR is a technique sensitive to the electron density depth profile of films and to the surface/interface roughness. The analysis of XRR curves collected for films of different thickness (from 1 to 30 nm) reveals a different growth mode for the two molecules as visualized by AFM measurements. **Figure 5** shows a series of XRR curves recorded for the a) PDIF-CN₂ and b) PDI8-CN₂ films with different thickness (from 1 to 30 nm).

Important information can be obtained from a general overview of the XRR curves: specifically, up to 10 nm, the XRR curves of the PDIF-CN₂ films exhibit Kiessig fringes' amplitude much larger than those observed for the corresponding PDI8-CN₂ films. These fringes, generated by the constructive interference between the X-ray beam reflected by the film surface and film/substrate interface, are an index of greater surface smoothness. The experimental XRR profiles have been reproduced by assuming that both OS films consist of a repetition of molecular layers, each one composed by three sub-monolayers of different heights and electron densities: two corresponding to the alkyl/fluoroalkyl chains and a central one to the aromatic core (Figure S8, Supporting Information). Due to the higher atomic weight of the PDIF-CN₂ lateral chains, compare to PDI8-CN₂, the electron density variation within each OS layer along the direction perpendicular to the substrate is more pronounced for PDIF-CN₂ than for PDI8-CN₂, which produces marked oscillations. The electron density depth profiles which best reproduce the experimental XRR curves are reported in Figure 5c and in Figure S9 (Supporting Information). For each PDIF-CN₂ film (a) all the OS layers have a constant density, indicating they are complete,

except the outermost surface layer which exhibits a substantial density reduction, suggesting an almost layer-by-layer growth mode. The 2D growth mode is maintained up to 30 nm, where only 2 uncompleted layers close to the interface with the electrolyte on top of 15 stacked molecular layers result from the best-fit of XRR curve (black curve Figure 5c). Conversely, for the PDI8-CN₂ films, the XRR curves could be well reproduced only by introducing several uncompleted sub-monolayers for each thickness value of the semiconductor, as highlighted by the slow decrease of the electron density depth profile (see Figure S9 in the Supporting Information for the 2 nm thick layer and the red curve in Figure 5c for the 30 nm thick layer). This result suggests that the PDI8-CN₂ molecules grow in a more 3D modality.

Since the dimension and shape of the grains as well as the number of outermost uncomplete layers (i.e., the *interfacial-portion* of the film) are thickness-independent in the case of PDIF-CN₂, the increase of charge mobility with the overall layer thickness must relate to the increase in the number of buried complete monolayers. Thus, it is plausible to consider the PDIF-CN₂ bulk-portion as a dense three-dimensional layered structure with each layer decoupled and independent to others due to the presence of fluorocarbon chains.^[53] This structure of the PDIF-CN₂ film comprised by alternated π -conjugated and insulating fluorocarbon layers can be described according to the model proposed by Sharma et al. for rationalizing the non-two-dimensional nature of the charge transport on the channel of organic FETs.^[54] It is plausible that charges are likely to delocalize in each of these uncoupled molecular layers rather than being only accumulated at the very interface with the electrolyte, thus enabling additional pathways for transport upon increasing the thickness of the semiconductor. In this scenario, the increase of current intensity and, consequently, of mobility in PDIF-CN₂ devices might be explained. The non-interacting layer-by-layer model cannot be applicable in case of the 3D growth mechanism due to large island formation which leads to a film structure not approximated to a dense three-dimensional layered structure. Thus, the mobility for PDI8-CN₂ devices is independent of the active layer thickness since the number of π -conjugated FET transporting layers, thus saturating between 10 and 15 nm.

Up to a 30 nm film thickness, it is possible to invoke a bulk-like conduction for PDIF-CN₂ WGO FET devices because the almost 2D layer-by-layer growth modality is preserved. Indeed, above 30 nm the mobility of PDIF-CN₂ drops by one order of magnitude (see Table 1), down to 10^{-6} cm² V⁻¹ s⁻¹ for 50 nm-thick film. An AFM image of a 40 nm-thick PDIF-CN₂ (Figure 6) clearly shows that the PDIF-CN₂ morphology is comprised of 3D structures such as needle-like grains mixed to few regions where the almost 2D structures (round terraces) are visible. The needle-like grains present in a region near to the 2D round terraces in the 40 nm-thick PDIF-CN₂ are 10 nm thick (Figure S10, Supporting Information) highlighting that also the surface morphology is affected by the change in the growth modality in the case of PDIF-CN₂ films. The drop of charge mobility for thicknesses larger than 30 nm corroborates the hypothesis that in PDIF-CN₂ the charge mobility increases with the OS film thickness as long as a packed layered growth modality is preserved.

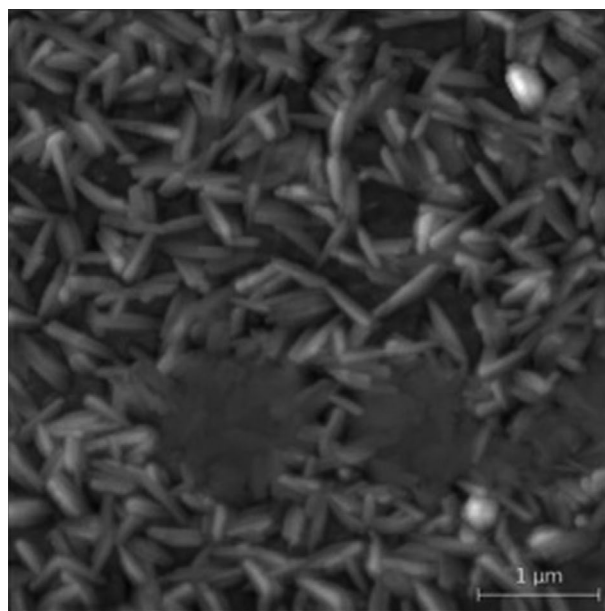


Figure 6. AFM image, $5 \times 5 \mu\text{m}^2$, of a 40 nm PDIF-CN₂ film: the growth modality changes from almost 2D (round terraces) to more 3D (grain with needle shape). Morphology is similar to that one of a 30 nm PDI8-CN₂ film; however, it is still possible to observe areas with round terraces.

3. Conclusions

In this work, we have presented for the first time the use of two small-molecule electron-transporting PDI derivatives, named PDIF-CN₂ and PDI8-CN₂, as semiconductors in WGO FETs. The two molecules differ only for the *N*-functionalization, partially fluorinated-chain for PDIF-CN₂ and alkyl-chain for PDI8-CN₂, while presenting identical solid-state arrangements. Both molecules show an FET behavior in WGO FET configuration but with different electron mobility values: for PDI8-CN₂ $\approx 10^{-4}$ cm² V⁻¹ s⁻¹ and up to 4.7×10^{-3} cm² V⁻¹ s⁻¹ for PDIF-CN₂, comparable to that of the state-of-the-art hole-transporting WGO FETs. The film growth modality was investigated for both semiconductors. PDI8-CN₂ shows a more 3D growth consistent with an OS film-thickness independent mobility. Differently, in the case of PDIF-CN₂, an almost 2D growth takes place initially, which is maintained with the increase of the thickness. Concomitantly, the electron mobility increases with the film thickness as long as an almost 2D growth is preserved, i.e., up to ≈ 30 nm. Above this value, PDIF-CN₂ switches to a more 3D growth, with the presence of needle-like grains on the surface, and the electron mobility drops down. Cross-correlating experimental data and theoretical modeling indicates that the crystallinity and *N*-substituents are not the causes of the enhanced charge transport of PDIF-CN₂ based WGO FETs. Considering the structural data obtained by XRR analysis, we can model the PDIF-CN₂ thin-film system as a dense layered structure in which each layer is decoupled from the others due to the presence of fluorocarbon chains. In this scenario, the availability of additional pathways for charge transport from buried layers upon increasing the film thickness might explain the mobility increase of PDIF-CN₂ with respect to PDI8-CN₂. Thus, the switch from a 2D to a 3D growth modality only stops this availability.

4. Experimental Section

Materials: *N,N'*-1H,1H-perfluorobutyl-dicyanoperylene-3,4:9,10-bis(dicarboximide) (PDIF-CN₂, FlexterraActivInk N1100) and *N,N'*-bis(*n*-octyl)-dicyanoperylene-3,4:9,10-bis(dicarboximide) (PDI8-CN₂, FlexterraActivInk N1200) were used as received from Flexterra Corp, Skokie, IL, US.

Device Processing: The WGFET devices were prepared onto Si/SiO₂ substrates purchased from Fondazione Bruno Kessler (Trento, Italy). The SiO₂ layer was 200 nm thick and thermally grown. Source (S) and Drain (D) gold electrodes (150 nm thick) exhibited a photolithographically defined interdigitated geometry with channel lengths (*L*) of 20 and 40 μm and width (*W*) of 11.2 and 22.4 μm, respectively. The substrates were cleaned three times in acetone and one time in isopropanol under ultrasonication; after the cleaning, the substrate surface was treated with hexamethyldisilazane (HMDS) purchased from Sigma-Aldrich Chemical Co. by exposing the substrates for 2 h to HMDS vapor in a low vacuum chamber. A thiol treatment by dip-coating follows the HMDS process: 4-chlorobenzenemethanethiol was used as 10 × 10⁻³ M thiol solution with ethanol (Sigma-Aldrich, >99.8%), the substrates were dipped for 1 min. The organic film was deposited in a high vacuum chamber by thermal sublimation with a rate of 0.6 nm min⁻¹ in a Knudsen cell. The substrate temperature was kept 90 °C during materials deposition.

Device Characterization: Water-gated electrical measurements were performed by a home-built system where the water has been confined on top of the devices by means of a plastic pool to guarantee high repeatability. The pool was filled with ultrapure deionized water working as electrolyte while the top gate consisted of a thin platinum wire (diameter 0.5 mm) that was immersed in the liquid. Source, drain, and gate electrodes were connected to an Agilent B1500A analyzer. The *I*/*V* saturation transfer curves were performed by sweeping the top gate-source voltage (*V*_{GS}) from -0.2 to 0.5 V while leaving the drain-source voltage (*V*_{DS}) constant at 0.5 V (saturation regime) and the substrate connected to ground. The *I*/*V* multiple output curves were carried out by sweeping *V*_{DS} from 0 to 0.5 V and *V*_{GS} from 0 to 0.5 V with a step of 0.1 V. Electrical parameters (mobility and threshold voltage) were calculated in a saturation regime from saturation transfer curve (STC).

Electrochemical Impedance Spectroscopy: Electrochemical impedance spectroscopy (EIS) experiments were performed on metal/electrolyte/semiconductor/metal stack architectures in potentiostatic mode with a two-electrode electrochemical cell on Autolab PGSTAT 128N Electrochemical Analyzer (USA METROHM Company). The organic semiconductor-coated Au electrode serves as the counter electrode while the top platinum electrode is the working electrode. High purity Milli-Q water is used in all the experiments as the electrolyte. The measurements are conducted spanning the frequency range from 0.7 Hz to 1 MHz with an AC amplitude of 500 mV. A DC bias voltage of 0 V is applied during the impedance measurement to fix the voltage potentials. The complex impedance *Z* used to determine the fitting parameters by means of an electrical equivalent circuit (see the Supporting Information) is determined as $Z = Z' + iZ''$, where *Z'* and *Z''* are the real and imaginary parts of the impedance, respectively.

Structural Characterization: Grazing incidence X-ray diffraction (GIXRD) measurements were performed at the ELETTRA-XRD1 beam line at Trieste's synchrotron facility (Italy) using a monochromatic beam with a wavelength (λ) of 1 Å and a dimension of 0.2 × 0.2 (H × V) mm². The incident angle of the X-ray beam was chosen 0.1°, slightly larger than the critical angle for total reflection of the organic film, in order to penetrate through the full film depth. The diffraction patterns were recorded using a 2D camera (Pilatus detector) placed normal to the incident beam direction at 400 mm from the sample. Specular scans (X-ray reflectivity and X-ray diffraction) were performed using a SmartLab-Rigaku diffractometer equipped with a rotating anode (Cu K α , $\lambda = 1.54180$ Å), followed by a parabolic mirror to collimate the incident beam, and a series of variable slits (placed before and after the sample position). XRR data were fitted and the electron density profile of films was determined using the *Gen X* software package.^[55]

Computational Details: The morphology of PDIF-CN₂ and PDI8-CN₂ was simulated by molecular dynamics (MD), using an interaction potential based on the OPLS force field.^[56] This computational approach reproduces the structure of molecular aggregates that are in excellent agreement with experiments.^[57–60] The water molecules were simulated using the TIP4P model. The Berendsen thermostat was used for simulations in the NVT and NPT with time constants of 0.1 and 1.0 ps, respectively. Coulomb interactions were accounted for by means of the particle mesh Ewald (PME) scheme, with a short-range cutoff of 1 nm.^[61] Simulations of layered systems were performed with 2D periodic models, applying periodic boundary conditions in 3D and inserting a vacuum region (about 20 Å) in the direction perpendicular to the molecular plane (*z*-axis). MD was performed by integrating the equation of motions with a finite time-step of 1 fs. Models of crystalline bilayers of PDIF-CN₂ and PDI8-CN₂ molecules, respectively, were initially built using the cell parameters present in literature, and subsequently equilibrating the systems for 1 ns at 300 K.^[21,25] Both the PDIF-CN₂ and PDI8-CN₂ 2D models were put in contact with water molecules and equilibrated at 300 K for 10 ns, computing structural parameters as averages of the last 5 ns. All the MD calculations were performed with the Gromacs program package.^[62] Density functional theory calculations were performed with the Siesta program package by applying the PBE gradient-corrected approximation to DFT and using a basis set of double- ζ plus polarization quality for orbital expansion and a mesh of 150 Ry for expansion of the electronic density.^[63]

Atomic Force Microscope Characterization: AFM characterizations were carried out using a hybrid system made of a commercial head (SMENA, NT-MDT), home-built electronics that can operate in several modes, and a digital lock-in amplifier (Zurich HF2LI). Specifically, characterizations were performed in Intermittent Contact mode. The employed cantilevers are commercially available from MikroMasch (HQ:NSC35).

Supporting Information

Supporting Information is available from the Wiley Online Library or from the author.

Acknowledgements

This work received funding from European Union's Horizon 2020 research and innovation program under grant agreement No.780839 (MOLOKO project). In addition, the authors wish to thank Vincenzo Ragona for the technical support. A.F. thanks AFOSR (FA9550-18-1-0320) for support.

Conflict of Interest

The authors declare no conflict of interest.

Keywords

electron-transporting semiconductors, field-effect mobility, growth modalities, rylene diimide, water-gated-organic field-effect transistors

Received: June 19, 2020

Revised: September 12, 2020

Published online: November 9, 2020

[1] T. Cramer, A. Campana, F. Leonardi, S. Casalini, A. Kyndiah, M. Murgia, F. Biscarini, *J. Mater. Chem. B* **2013**, *1*, 3728.

[2] D. Wang, V. Noël, B. Piro, *Electronics* **2016**, *5*, 9.

- [3] M. Y. Mulla, E. Tuccori, M. Magliulo, G. Lattanzi, G. Palazzo, K. Persaud, L. Torsi, *Nat. Commun.* **2015**, *6*, 6010.
- [4] E. Macchia, K. Manoli, B. Holzer, C. Di Franco, R. A. Picca, N. Cioffi, G. Scamarcio, G. Palazzo, L. Torsi, *Anal. Bioanal. Chem.* **2019**, *411*, 4899.
- [5] T. Cramer, A. Kyndiah, M. Murgia, F. Leonardi, S. Casalini, F. Biscarini, *Appl. Phys. Lett.* **2012**, *100*, 143302.
- [6] L. Kergoat, L. Herlogsson, D. Braga, B. Piro, M. C. Pham, X. Crispin, M. Berggren, G. Horowitz, *Adv. Mater.* **2010**, *22*, 2565.
- [7] M. Muccini, *Nat. Mater.* **2006**, *5*, 605.
- [8] M. Muccini, S. Toffanin, *Organic Light-Emitting Transistors: Towards the Next Generation Display Technology*, Wiley-Science Wise Co-Publication, Hoboken, NJ **2016**.
- [9] H. Schlaich, M. Muccini, J. Feldmann, H. Bässler, E. O. Göbel, R. Zamboni, C. Taliani, J. E. Erxmeier, A. Weidinger, *Chem. Phys. Lett.* **1995**, *236*, 135.
- [10] T. Benincori, M. Capaccio, F. De Angelis, L. Falciola, M. Muccini, P. Mussini, A. Ponti, S. Toffanin, P. Traldi, F. Sannicolò, *Chem. - Eur. J.* **2008**, *14*, 459.
- [11] A. Köhler, H. Bässler, *Electronic Process in Organic Semiconductor. An Introduction*, Wiley, Weinheim, Germany **2015**.
- [12] M. A. Loi, E. D. A. Como, F. Dinelli, M. Murgia, R. Zamboni, F. Biscarini, M. Muccini, *Nat. Mater.* **2005**, *4*, 81.
- [13] P. Mei, M. Murgia, C. Taliani, E. Lunedei, M. Muccini, *J. Appl. Phys.* **2000**, *88*, 5158.
- [14] F. Dinelli, M. Murgia, P. Levy, M. Cavallini, F. Biscarini, D. M. De Leeuw, *Phys. Rev. Lett.* **2004**, *92*, 90.
- [15] L. Kergoat, B. Piro, M. Berggren, G. Horowitz, M. C. Pham, *Anal. Bioanal. Chem.* **2012**, *402*, 1813.
- [16] M. Melucci, M. Durso, C. Bettini, M. Gazzano, L. Maini, S. Toffanin, S. Cavallini, M. Cavallini, D. Gentili, V. Biondo, G. Generali, F. Gallino, R. Capelli, M. Muccini, *J. Mater. Chem. C* **2014**, *2*, 3448.
- [17] M. Melucci, L. Favaretto, M. Zambianchi, M. Durso, M. Gazzano, A. Zanelli, M. Monari, M. G. Lobello, F. De Angelis, V. Biondo, G. Generali, S. Troisi, W. Koopman, S. Toffanin, R. Capelli, M. Muccini, *Chem. Mater.* **2013**, *25*, 668.
- [18] H. Sirringhaus, *Adv. Mater.* **2005**, *17*, 2411.
- [19] M. Mas-Torrent, C. Rovira, *Chem. Soc. Rev.* **2008**, *37*, 827.
- [20] E. Benvenuti, D. Gentili, F. Chiarella, A. Portone, M. Barra, M. Cecchini, C. Cappuccino, M. Zambianchi, S. G. Lopez, T. Salzillo, E. Venuti, A. Cassinese, D. Pisignano, L. Persano, M. Cavallini, L. Maini, M. Melucci, M. Muccini, S. Toffanin, *J. Mater. Chem. C* **2018**, *6*, 5601.
- [21] F. Liscio, S. Milita, C. Albonetti, P. D'Angelo, A. Guagliardi, N. Masciocchi, R. G. Della Valle, E. Venuti, A. Brillante, F. Biscarini, *Adv. Funct. Mater.* **2012**, *22*, 943.
- [22] B. A. Jones, A. Facchetti, M. R. Wasielewski, T. J. Marks, *J. Am. Chem. Soc.* **2007**, *129*, 15259.
- [23] X. Zhan, A. Facchetti, S. Barlow, T. J. Marks, M. A. Ratner, M. R. Wasielewski, S. R. Marder, *Adv. Mater.* **2011**, *23*, 268.
- [24] M. Barra, F. Chiarella, F. Chianese, R. Vaglio, A. Cassinese, *Electron* **2019**, *8*, 249.
- [25] V. Belova, B. Wagner, B. Reisz, C. Zeiser, G. Duva, J. Rozbořil, J. Novák, A. Gerlach, A. Hinderhofer, F. Schreiber, *J. Phys. Chem. C* **2018**, *122*, 8589.
- [26] A. Laiho, L. Herlogsson, R. Forchheimer, X. Crispin, M. Berggren, *Proc. Natl. Acad. Sci. USA* **2011**, *108*, 15069.
- [27] A. Sharma, S. G. J. Mathijssen, T. Cramer, M. Kemerink, D. M. De Leeuw, P. A. Bobbert, *Appl. Phys. Lett.* **2010**, *96*, 103306.
- [28] F. Buth, D. Kumar, M. Stutzmann, J. A. Garrido, *Appl. Phys. Lett.* **2011**, *98*, 153302.
- [29] M. E. Roberts, S. C. B. Mannsfeld, M. L. Tang, Z. Bao, *Chem. Mater.* **2008**, *20*, 7332.
- [30] S. Ono, N. Minder, Z. Chen, A. Facchetti, A. F. Morpurgo, *Appl. Phys. Lett.* **2010**, *97*, 143307.
- [31] A. Malti, E. O. Gabriëlsson, M. Berggren, X. Crispin, *Appl. Phys. Lett.* **2011**, *99*, 063305.
- [32] R. Porrazzo, A. Luzio, S. Bellani, G. E. Bonacchini, Y. Y. Noh, Y. H. Kim, G. Lanzani, M. R. Antognazza, M. Caironi, *ACS Omega* **2017**, *2*, 1.
- [33] A. S. Molinari, H. Alves, Z. Chen, A. Facchetti, A. F. Morpurgo, *J. Am. Chem. Soc.* **2009**, *131*, 2462.
- [34] M. Barra, F. V. Di Girolamo, N. A. Minder, I. Gutiérrez Lezama, Z. Chen, A. Facchetti, A. F. Morpurgo, A. Cassinese, *Appl. Phys. Lett.* **2012**, *100*, 133301.
- [35] S. Fabiano, H. Wang, C. Piliago, C. Jaye, D. A. Fischer, Z. Chen, B. Pignataro, A. Facchetti, Y. L. Loo, M. A. Loi, *Adv. Funct. Mater.* **2011**, *21*, 4479.
- [36] B. A. Jones, A. Facchetti, M. R. Wasielewski, T. J. Marks, *Adv. Funct. Mater.* **2008**, *18*, 1329.
- [37] J. Youn, G. R. Dholakia, H. Huang, J. W. Hennek, A. Facchetti, T. J. Marks, *Adv. Funct. Mater.* **2012**, *22*, 1856.
- [38] F. Chiarella, M. Barra, A. Carella, L. Parlato, E. Sarnelli, A. Cassinese, *Org. Electron.* **2016**, *28*, 299.
- [39] J. Rivnay, L. H. Jimison, J. E. Northrup, M. F. Toney, R. Noriega, S. Lu, T. J. Marks, A. Facchetti, A. Salleo, *Nat. Mater.* **2009**, *8*, 952.
- [40] B. A. Jones, M. J. Ahrens, M. H. Yoon, A. Facchetti, T. J. Marks, M. R. Wasielewski, *Angew. Chem., Int. Ed.* **2004**, *43*, 6363.
- [41] J. Soeda, T. Uemura, Y. Mizuno, A. Nakao, Y. Nakazawa, A. Facchetti, J. Takeya, *Adv. Mater.* **2011**, *23*, 3681.
- [42] Q. Zhang, F. Leonardi, S. Casalini, I. Temiño, M. Mas-Torrent, *Sci. Rep.* **2016**, *6*, 39623.
- [43] H. Schamoni, S. Noever, B. Nickel, M. Stutzmann, J. A. Garrido, *Appl. Phys. Lett.* **2016**, *108*, 073301.
- [44] M. Barra, D. Viggiano, P. Ambrosino, F. Bloisi, F. V. Di Girolamo, M. V. Soldovieri, M. Tagliatalata, A. Cassinese, *Biochim. Biophys. Acta, Gen. Subj.* **2013**, *1830*, 4365.
- [45] S. H. Lee, P. J. Rossky, *J. Chem. Phys.* **1994**, *100*, 3334.
- [46] K. Willa, R. Häusermann, T. Mathis, A. Facchetti, Z. Chen, B. Batlogg, *J. Appl. Phys.* **2013**, *113*, 133707.
- [47] A. S. Molinari, H. Alves, Z. Chen, A. Facchetti, A. F. Morpurgo, *J. Am. Chem. Soc.* **2009**, *131*, 2462.
- [48] M. Di Lauro, M. Berto, M. Giordani, S. Benaglia, G. Schweicher, D. Vuillaume, C. A. Bortolotti, Y. H. Geerts, F. Biscarini, *Adv. Electron. Mater.* **2017**, *3*, 1700159.
- [49] R. Ruiz, A. Papadimitratos, A. C. Mayer, G. G. Malliaras, *Adv. Mater.* **2005**, *17*, 1795.
- [50] F. Chiarella, M. Barra, L. Ricciotti, A. Aloisio, A. Cassinese, *Electron* **2014**, *3*, 76.
- [51] F. V. Di Girolamo, F. Ciccullo, M. Barra, A. Carella, A. Cassinese, *Org. Electron.* **2012**, *13*, 2281.
- [52] P. G. De Gennes, F. Brochard-Wyart, D. Quere, *Capillarity and Wetting Phenomena Drops, Bubbles, Pearls, Waves*, Springer-Verlag, New York **2004**.
- [53] N. A. Minder, S. Ono, Z. Chen, A. Facchetti, A. F. Morpurgo, *Adv. Mater.* **2012**, *24*, 503.
- [54] A. Sharma, F. W. A. Van Oost, M. Kemerink, P. A. Bobbert, *Phys. Rev. B: Condens. Matter Mater. Phys.* **2012**, *85*, 235302.
- [55] M. Björck, G. Andersson, *J. Appl. Crystallogr.* **2007**, *40*, 1174.
- [56] W. L. Jorgensen, D. S. Maxwell, J. Tirado-Rives, *J. Am. Chem. Soc.* **1996**, *118*, 11225.
- [57] A. Lorenzoni, M. Muccini, F. Mercuri, *Adv. Theory Simul.* **2019**, *2*, 1900156.
- [58] A. Lorenzoni, M. Muccini, F. Mercuri, *RSC Adv.* **2015**, *5*, 11797.
- [59] A. Lorenzoni, M. Muccini, F. Mercuri, *J. Phys. Chem. C* **2017**, *121*, 21857.
- [60] A. Lorenzoni, A. Mosca Conte, A. Pecchia, F. Mercuri, *Nanoscale* **2018**, *10*, 9376.
- [61] T. Darden, D. York, L. Pedersen, *J. Chem. Phys.* **1993**, *98*, 10089.
- [62] D. Van Der Spoel, E. Lindahl, B. Hess, G. Groenhof, A. E. Mark, H. J. C. Berendsen, *J. Comput. Chem.* **2005**, *26*, 1701.
- [63] J. M. Soler, E. Artacho, J. D. Gale, A. García, J. Junquera, P. Ordejón, D. Sánchez-Portal, *J. Phys.: Condens. Matter* **2002**, *14*, 2745.